RSC Advances

PAPER

View Article Online
View Journal | View Issue

Cite this: *RSC Adv.*, 2015, **5**, 103421

Ordered mesoporous carbons-supported gold nanoparticles as highly efficient electrocatalysts for oxygen reduction reaction†

Likai Wang,[a] Zhenghua Tang,*[ab] Xiaojun Liu,[a] Wenhan Niu,[a] Kai Zhou,[a] Hongyu Yang,[a] Weijia Zhou,[a] Ligui Li[a] and Shaowei Chen*[ac]

Received 9th October 2015
Accepted 25th November 2015

DOI: 10.1039/c5ra20955b

www.rsc.org/advances

Unlike bulk gold, gold nanoparticles (AuNPs) have been found to exhibit apparent electrocatalytic activity for oxygen reduction reaction (ORR). In this work, glutathione-capped AuNPs of *ca.* 4 nm in diameter were prepared by a wet chemical method and embedded into a mesoporous carbon matrix synthesized by using an SBA-15 amorphous silica template. Pyrolysis at elevated temperatures led to removal of the organic capping ligands and the formation of ordered mesoporous carbons loaded with a selected amount of AuNPs which exhibited no apparent agglomeration. The obtained nanocomposites exhibited apparent ORR activity in alkaline media, and the sample with 20 wt% AuNPs stood out as the best among the series, within the context of onset potential, kinetic current density and stability, in comparison with AuNPs alone, ordered mesoporous carbons, and commercial Pt/C catalysts. The remarkable performance was ascribed to the intimate interactions between the AuNPs and mesoporous carbons that facilitated fast electron transfer and rapid mass transport. This is the first time that ordered mesoporous carbons were employed to support AuNPs as ORR catalysts. The strategy may be exploited to prepare a wide range of electrocatalysts based on mesoporous carbons-supported metal nanoparticles with extraordinary reactivity and enhanced stability for ORR.

Introduction

Fuel cell technologies, in particular, proton exchange membrane fuel cells (PEMFCs), have been attracting extensive interest due to their high energy density, low operation temperature, as well as minimal negative environmental impacts.[1,2] One critical issue of research is to develop efficient electrocatalysts for both oxidation of small organic fuel molecules at the anode and reduction of oxygen at the cathode so as to achieve a sufficiently high current density needed for practical applications.[3] In particular, because of the sluggish electron-transfer kinetics and complex reaction pathways, oxygen reduction reaction (ORR) has been recognized as a major bottleneck that limits the fuel cell performance. It has been well recognized that Pt and Pt-based alloys[4–9] are the catalysts of choice for both hydrogen oxidation and oxygen reduction in PEMFCs. However, the limited reserves of Pt in the nature and the resulting high costs[10] have severely hindered large-scale commercial applications of fuel cells. Therefore, extensive research efforts have been devoted to the development of alternative catalysts that are viable and competitive, as compared to Pt.[11–15]

With a filled d band and high activation energy barrier, bulk gold has been considered to bear poor catalytic activity as manifested in both experimental studies and density functional theory (DFT) calculations.[16] However, a series of recent studies have shown that AuNPs exhibited apparent catalytic activity in CO oxidation,[17–19] selective oxidation of organic molecules,[20–22] and ORR,[23–25] in sharp contrast with bulk Au. Such unique catalytic behaviors are primarily attributed to the high fraction of surface atoms with low coordination numbers.[10,23,26] In fact, strong core size effects have been observed of AuNPs on the kinetics of oxygen reduction, where the activity increased with decreasing AuNP core size.[16,23,27] Unfortunately, when small-sized Au catalysts are employed alone, they are unstable and tend to dissolve and aggregate into larger particles due to Ostwald ripening.[16] Therefore, to improve their stability, extensive research has been carried out where AuNPs are confined on specific supports, such as graphene,[26,27] TiO_2,[28] and CeO_2.[29,30] Among these, ordered porous carbons with a uniform pore structure, large specific pore volume and high effective surface area have attracted particular interest, largely because of their

[a]*New Energy Research Institute, School of Environment and Energy, South China University of Technology, Guangzhou Higher Education Mega Center, Guangzhou, 510006, P. R. China. E-mail: zhht@scut.edu.cn*

[b]*Guangdong Provincial Key Laboratory of Atmospheric Environment and Pollution Control, Guangzhou, Guangdong, 510006, P. R. China*

[c]*Department of Chemistry and Biochemistry, University of California, 1156 High Street, Santa Cruz, California 95064, USA. E-mail: shaowei@ucsc.edu*

† Electronic supplementary information (ESI) available: UV-visible spectra of AuNPs, additional TEM and SEM images of Z-SBA15, high-resolution XPS spectra of Au 4f and C 1s electrons. See DOI: 10.1039/c5ra20955b

environmental friendliness, low costs, super long durability, and robust stability toward CH_3OH poisoning.[31,32]

Herein, for the first time ever, nanocomposites based on AuNPs supported on ordered mesoporous carbons were prepared and used as electrocatalysts for ORR. AuNPs with a narrow size distribution were synthesized and embedded into ordered mesoporous carbons. The intimate interactions between the AuNPs and porous carbons helped prevent the agglomeration of AuNPs during pyrolysis, leading to enhanced exposure of catalytically active sites, fast electron transfer and rapid mass transport of reaction species. The sample with a 20 wt% AuNPs loading was found to exhibit the best electrocatalytic performance among the series, within the context of onset potential, ORR kinetic current density, and stability, as compared with AuNPs, mesoporous carbons, and commercial Pt/C.

Experimental section

Materials

Hydrogen tetrachloroaurate(III) trihydrate ($HAuCl_4 \cdot 3H_2O$) and reduced L-glutathione were purchased from Energy Chemicals (Shanghai, China), while sodium borohydride ($NaBH_4$) and SBA-15 amorphous silica were acquired from Aladdin Industrial Corporation (Shanghai, China). Sucrose was purchased from Sinopharm Chemical Reagents Beijing Co. 20 wt% Pt/C was purchased from Alfa Aesar. Water was supplied with a Barnstead Nanopure Water System (18.3 MΩ cm). All chemicals were used as received without further purification.

Preparation of mesoporous carbons

Mesoporous carbons were prepared by following a previous synthetic procedure.[33] Briefly, 1 g of SBA-15 amorphous silica was added into an aqueous solution prepared by dissolving 1.25 g of sucrose and 0.14 g of H_2SO_4 in 5 mL of H_2O in a 50 mL Teflon lined autoclave. The mixture was kept at 373 K for 6 h in an oven, and at 433 K for another 6 h. The sample was found to turn dark brown during the heating treatment in the oven. The resultant sample was repeatedly heated following the above procedure after the addition of 0.8 g sucrose, 0.09 g H_2SO_4 and 5 g H_2O. The obtained samples then underwent pyrolysis at 900 °C for 5 h, leading to the formation of carbon–silica composites, which were immersed in a 10 wt% HF solution for 24 h to remove the silica template, affording mesoporous carbons which displayed ordered trenches of *ca.* 10 nm in diameter and several microns in length. The resulting materials were denoted as Z-SBA15 (Fig. S1†).

Synthesis of AuNPs

AuNPs were synthesized by adopting a literature protocol.[34] Briefly, 104 mg of $HAuCl_4 \cdot 3H_2O$ was added to 52 mL of H_2O in a round-bottom flask, and the resulting solution was cooled to 0 °C in an ice bath over a period of 30 min. 324 mg of glutathione was added slowly into the flask under slow magnetic stirring (~100 rpm). The solution gradually became colorless after continuous stirring for 2 h. A freshly prepared $NaBH_4$ solution (100 mg, dissolved in 13 mL of ice-cold water) was rapidly added to the solution under vigorous stirring (1200 rpm), where the solution color changed quickly to dark brown, signifying the formation of gold nanoparticles. The reaction was allowed to proceed for about 12 h before 32 mL of methanol was slowly added under stirring, leading to the formation of a black precipitate which was collected by centrifugation (3800 rpm, 10 min) and repeatedly washed by methanol (5 mL × 3). TEM measurements showed that the average core diameter of the AuNPs was 4.6 ± 0.9 nm (Fig. S1†), and UV-visible measurements (Fig. S2†) displayed an apparent absorption peak at 520 nm, characteristic of gold nanoparticles due to the well-known surface plasmon resonance.

Preparation of mesoporous carbon-supported AuNPs

The procedure is depicted in Fig. 1. In a typical experiment, 40 mg of mesoporous carbons obtained above was added into 150 mL of H_2O in a round bottom flask. Separately, 10 mg of AuNPs prepared above was added to 20 mL of H_2O under constant stirring for 20 min. Then the solution of AuNPs was added dropwise to the porous carbon solution under vigorous stirring and sonicated for 3 h at room temperature. The solvents were then removed by rotary evaporation, and the obtained solids were denoted as AuMC-20%-no annealing. Such solids were then pyrolyzed at 600 °C for 2 h under a nitrogen flow, affording mesoporous carbon-supported gold nanoparticles in which the Au mass loading was 20%. This sample was referred to as AuMC-20%.

Samples of other Au loadings (10 and 30%) were also prepared in a similar fashion except that a different amount of AuNPs was mixed with the mesoporous carbons. These were denoted as AuMC-10% and AuMC-30%, respectively.

Characterizations

UV-visible absorption spectra were acquired with a Shimadzu 2600/2700 UV-visible scanning spectrophotometer using a 1 cm quartz cuvette. The sample morphology was examined with

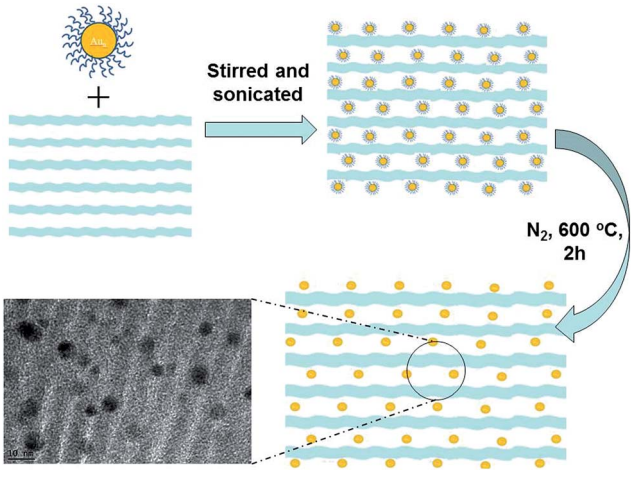

Fig. 1 Schematic illustration of the preparation of mesoporous carbon-supported AuNPs composites.

a high-resolution transmission electron microscope (JEOL JEM-2010), where TEM samples were prepared by dropcasting a catalyst dispersion directly onto a copper grid coated with a holey carbon film. Field-emission scanning electron microscopic (FESEM, NOVA NanoSEM 430, FEI) measurements were employed to characterize the morphologies of the as-prepared samples. Samples for FESEM analysis were prepared by dispensing several drops of a dilute catalyst dispersion in ethanol on a clean silicon (111) substrate. BET surface areas were determined with a Micromeritics ASAP 2010 instrument with nitrogen adsorption at 77 K using the Barrett–Joyner–Halenda (BJH) method. The pore-size distribution was calculated with a DFT method by using the nitrogen adsorption data and assuming a slit pore model. X-ray diffraction (XRD) patterns in the Bragg's angle (2θ) range of 10 to 80° were collected at room temperature by using a Bruker D8 diffractometer with Cu Kα radiation ($\lambda = 0.1541$ nm). X-ray photoelectron spectroscopy (XPS) analysis was carried out with a VG MultiLab 2000 instrument with a monochromatic Al Kα X-ray source (Thermo VG Scientific).

Electrochemical measurements

Electrochemical measurements were conducted with a CHI 750E electrochemical workstation (CH Instruments Inc.) in a 0.1 M KOH aqueous solution at room temperature. A platinum wire and a Ag/AgCl electrode were used as the counter electrode and reference electrode, respectively. The working electrode was a glassy carbon-disk electrode (diameter 5.61 mm) of an RRDE (with a collection efficiency of 37%) from Pine Instrument, Inc.[35] The working electrode was cleaned by mechanical polishing with aqueous slurries of 0.3 μm alumina powders on a polishing microcloth. The catalyst ink was prepared by adding 2 mg of a catalyst into 1.0 mL ethanol solution containing 10 μL Nafion (5 wt%, Aldrich). The catalyst ink (10 μL) was then drop-cast onto the glassy carbon disk and dried at room temperature, and the catalyst loading was calculated to be 80.8 μg cm^{-2} for all samples.

In all measurements, the Ag/AgCl reference electrode was calibrated with respect to a reversible hydrogen electrode (RHE). The calibration was performed in a high-purity H_2 (99.999%) saturated electrolyte with a Pt wire as both the working electrode and counter electrode. Cyclic voltammograms were collected at a scan rate of 10 mV s^{-1}, and the average of the two potentials at which the current crossed zero was taken as the thermodynamic potential for the hydrogen electrode reactions. In 0.1 M KOH, $E_{Ag/AgCl} = E_{RHE} + 0.966$ V.

Results and discussion

Fig. 1 depicts the schematic of the preparation of mesoporous carbon-supported AuNPs nanocomposites. First, AuNPs and mesoporous carbons were synthesized separately.[33,34] Then they were dispersed in water and mixed under vigorous stirring. Sonication led to efficient incorporation of AuNPs into the mesoporous carbons. The mixture was then calcined under a N_2 atmosphere at 600 °C, affording mesoporous carbon-supported AuNPs.

The embedding of AuNPs into the mesoporous carbon scaffolds can be readily seen in TEM measurements. From Fig. 2 where the AuNP loading ranged from 10 to 30 wt%, one can see that a number of dark-contrast objects (AuNPs) were embedded within low-contrast ordered one-dimensional trenches (carbon) without apparent agglomeration, and the average size of the nanoparticles remained almost unchanged as compared to that of the original nanoparticles (4.6 ± 0.9 nm, Fig. S1†). This suggests excellent protection of the AuNPs by the porous carbons even during high-temperature pyrolysis.

The structures of the nanocomposites were further evaluated by XRD measurements. From Fig. 3a, it can be seen that Z-SAB15 (green curve) exhibited two peaks at $2\theta = 26.0$ and 44.1°, which can be attributed to diffractions from the (002) and (101) planes of hexagonal carbon (JCPDS 75-1621), respectively. For AuMC-20% (black curve), in addition to the peak at 26.0° from Z-SBA15, a series of well-defined diffraction peaks at $2\theta =$ 38.3°, 44.4° (which overlaps with the C (101) peak), 64.7°, and 77.6° can also be observed. These are consistent with the (111), (200), (220), and (311) crystalline planes of fcc Au (JCPDS 65-2870). These results demonstrate that AuNPs were indeed dispersed into Z-SBA15. Further structural insights were obtained in XPS measurements. From Fig. 3b, the C 1s (284.8 eV) and O 1s (532.3 eV) peaks were well-defined in Z-SBA15 (green curve); and for the AuMC-20% sample (black curve), the Au 4f electrons (Au $4f_{5/2}$ and $4f_{7/2}$) can be easily identified at 84.4 eV and 88.1 eV as well, further confirming the incorporation of

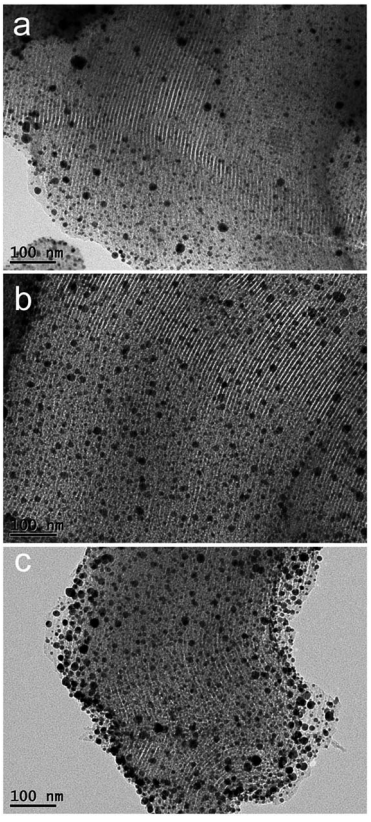

Fig. 2 Representative TEM images of (a) AuMC-10%, (b) AuMC-20%, and (c) AuMC-30%. Scale bars are all 100 nm.

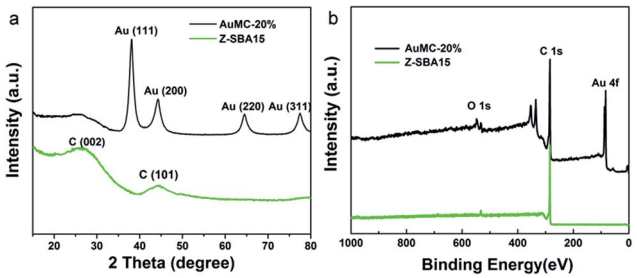

Fig. 3 (a) XRD patterns and (b) XPS survey spectra of AuMC-20% and Z-SBA15.

AuNPs in the hybrids. In addition, based on the integrated peak areas, the loading of Au in the AuMC-20% sample was estimated to be 3.7 at%.

The specific surface areas of the AuMC samples were then quantified by N_2 adsorption/desorption analysis. Fig. 4a depicts the adsorption isotherms of the three AuMC samples along with Z-SBA15, which all showed a type IV adsorption/desorption isotherm with a clear hysteresis loop in the relative pressure region of $P/P_0 = 0.4$–1.0, implying the formation of mesopores in the materials. Additionally, the specific surface area was quantified by the BJH method at 1110 $m^2\ g^{-1}$ for Z-SBA15, 979 $m^2\ g^{-1}$ for AuMC-10%, 875 $m^2\ g^{-1}$ for AuMC-20% and 823 $m^2\ g^{-1}$ for AuMC-30%, indicating a decrease of the effective surface area with increasing AuNPs loading. This is consistent with the TEM results presented in Fig. 2. Interestingly, the embedding of AuNPs did not seem to affect the pore size distribution significantly, as shown in Fig. 4b. In fact, the average pore diameter was very consistent among the samples, at 4.38 nm for Z-SBA15, 4.30 nm for AuMC-10%, 4.29 nm for AuMC-20% and 4.25 nm for AuMC-30%, indicating that indeed mesopores were formed within the samples which were known to facilitate mass transfer of reaction intermediates in ORR.[36,37]

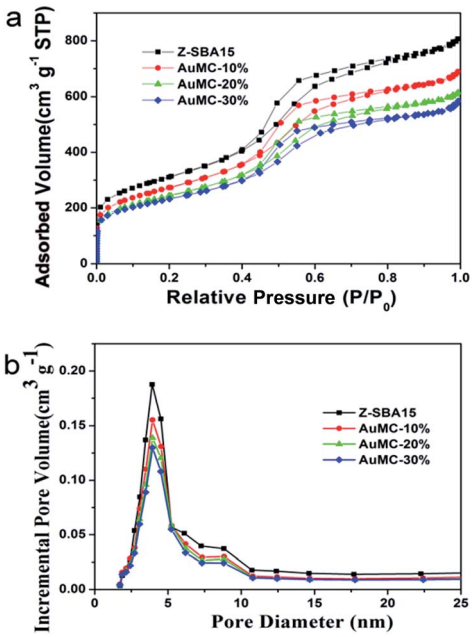

Fig. 4 (a) Nitrogen adsorption/desorption isotherms and (b) pore-size distributions of Z-SBA15, AuMC-10%, AuMC-20% and AuMC-30%.

Interestingly, the obtained hybrids exhibited apparent electrocatalytic reactivity for ORR. Fig. 5a depicts the cyclic voltammograms of a glassy carbon electrode modified with 20 μg of Z-SBA15 (black curve), AuNPs (red curve), AuMC-20%-no annealing (green curve), AuMC-20% (blue curve), and commercial Pt/C (cyan curve) in an oxygen-saturated 0.1 M KOH solution at room temperature at a potential scan rate of 10 mV s^{-1}. It can be seen that for all samples, as the electrode potential swept negatively past +1.0 V, a cathodic peak started to emerge, suggesting apparent electrocatalytic activity for oxygen reduction. Yet the onset (E_{onset}) and peak (E_p) potentials are clearly different among the samples. For instance, for the AuMC-20% sample, E_{onset} can be estimated to be +0.93 V (*vs.* RHE) and E_p = +0.85 V; for commercial Pt/C, E_{onset} = +0.95 V and E_p = +0.82 V, whereas for Z-SBA15, E_{onset} = +0.82 V and E_p = +0.76 V, for AuNPs alone, E_{onset} = +0.71 V and E_p = +0.61 V, and for AuMC-20%-no annealing, E_{onset} = +0.83 V and E_p = +0.78 V. Moreover, the peak current density also exhibits a distinct variation at 0.28 mA cm^{-2} for AuNPs, 0.45 mA cm^{-2} for Z-SBA15, 0.38 mA cm^{-2} for AuMC-20%-no annealing, 0.51 mA cm^{-2} for AuMC-20%, and 0.57 mA cm^{-2} for Pt/C. Note that the onset potential and peak current density are two key parameters in the quantitative assessments of the electrocatalytic performance. Taken together, these results suggest that AuMC-20% exhibited the best activity among the series of samples except Pt/C. Consistent results are obtained in RDE measurements (Fig. 5b). One can see that at +0.45 V, the limiting current density at 2500 rpm is 1.8 mA cm^{-2} for AuNPs, 2.6 mA cm^{-2} for Z-SBA15 and AuMC-20%-no annealing, 3.5 mA cm^{-2} for AuMC-20% and 5.0 mA cm^{-2} for Pt/C. These results are consistent with cyclic voltammetric measurements in Fig. 5a. The superior electrocatalytic activity of AuMC-20% for ORR may be attributed to the intimate electronic interactions between AuNPs and carbon support that promoted electron transfer and mass transport.[38,39]

The effects of Au loading on the ORR performance were also examined. Fig. 5c shows the RRDE voltammograms of a glassy-carbon disk electrode modified with AuMC-10%, AuMC-20%, and AuMC-30% in an oxygen-saturated 0.1 M KOH solution. It can be observed that all nanocomposites showed apparent ORR activity; yet the onset potential and limiting current density varied with the Au loading: +0.84 V and 3.95 mA cm^{-2} for 10%, +0.91 V and 4.35 mA cm^{-2} for 20%, and +0.89 V and 3.48 mA cm^{-2} for 30%. From these, one can see that the 20% sample, again, stood out as the best among the series (though somewhat subpar as compared to commercial Pt/C).

Fig. 5d shows the RRDE voltammograms of oxygen reduction recorded at the AuMC-20% electrode in an oxygen-saturated 0.1 M KOH solution at different rotation rates (from 100 to 2500 rpm). It can be seen that the voltammetric currents increased with increasing electrode ration rate. Based on the RRDE measurements, the number of electron transfer (n) during the ORR could be calculated according to eqn (1),

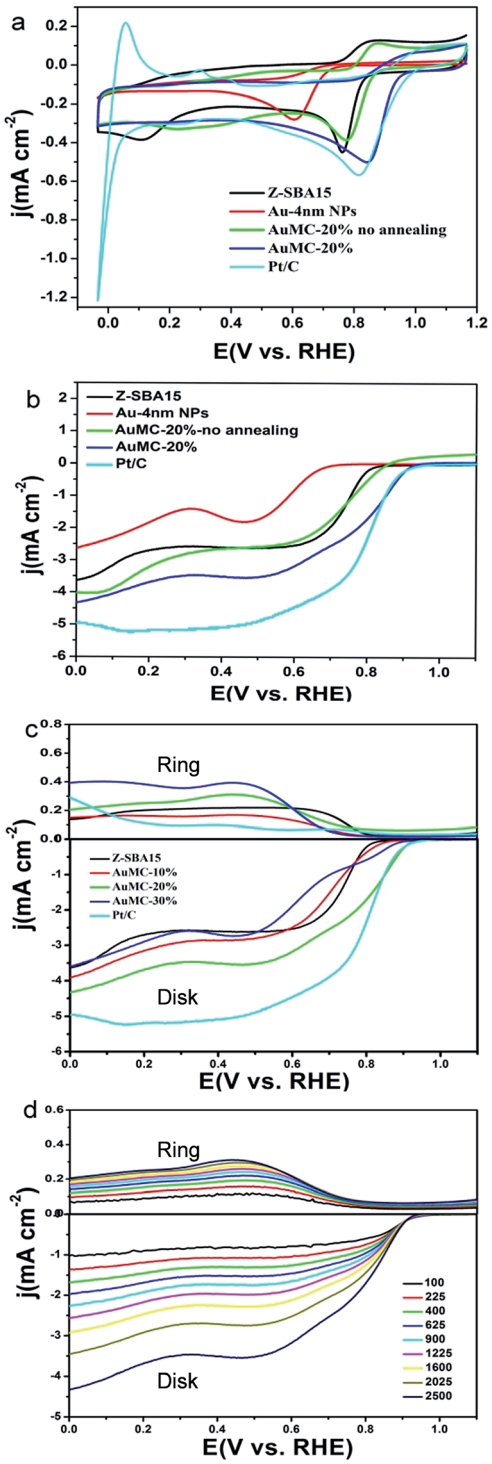

Fig. 5 (a) Cyclic and (b) RDE voltammograms at 2500 rpm of Z-SBA15 (black curve), AuNPs (red curve), AuMC-20%-no annealing (green curve), AuMC-20% (blue curve), and Pt/C (cyan curve) on a glassy carbon electrode in O_2-saturated 0.1 M KOH. (c) RRDE voltammograms of Z-SBA15, AuMC-10%, AuMC-20%, AuMC-30% and Pt/C in O_2-saturated 0.1 M KOH at 2500 rpm. (d) RRDE voltammograms of AuMC-20% in O_2-saturated 0.1 M KOH at different rotation speeds (in rpm, as specified in figure legends). Potential scanning rates all 10 mV s^{-1}.

$$n = \frac{4I_d}{I_d + I_r/N} \quad (1)$$

where I_d is the disk current, I_r is the ring current, and N is the RRDE collection efficiency (0.37). The variation of the n values *versus* electrode potential for the varied catalysts is presented in Fig. 6a. For AuMC-30%, the n value was approximately 3.0 within the potential range of 0 to +0.5 V, implying that ORR proceeded by a mix of two- and four-electron reduction pathways. The n values of AuMC-10% and AuMC-20% were somewhat higher at 3.1–3.5 and 3.2–3.5 in the same potential range, implying the best ORR performance with the AuMC-20% sample, although still lower than that of commercial Pt/C (*ca.* 3.8). The corresponding Tafel plots are depicted in Fig. 6b. A similar slope was observed for AuMC-10% (58.3 mV dec^{-1}), AuMC-20% (62.5 mV dec^{-1}), AuMC-30% (67.8 mV dec^{-1}) and Pt/C (57.2 mV dec^{-1}), which indicated a similar reaction mechanism of ORR on the catalyst surface where the rate-determining step at the catalysts was likely the first electron

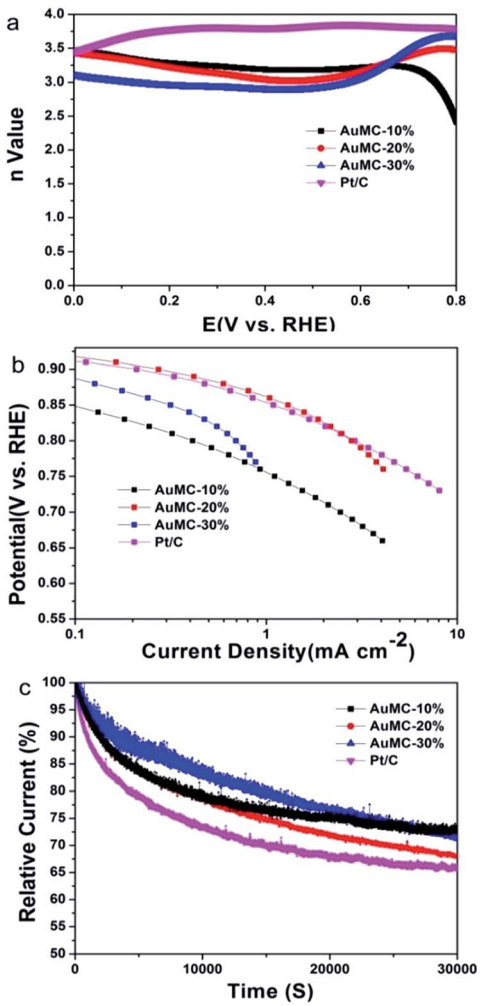

Fig. 6 (a) n-Values of AuMC-10%, AuMC-20%, AuMC-30% and Pt/C *versus* potential. (b) Tafel plots of AuMC-10%, AuMC-20%, AuMC-30% and Pt/C. (c) Chronoamperometric responses for ORR at AuMC-10%, AuMC-20%, AuMC-30% and Pt/C electrodes in an O_2-saturated 0.1 M KOH solution at +0.5 V for 30 000 s.

reduction of oxygen.[36,37] Note that we repeated the synthesis and tests of each sample at least three times, and the results were highly reproducible for each sample (Fig. S3†), with AuMC-20% consistently being the best among the series. Importantly, the kinetic current density (specific activity) of the AuMC-20% sample was highly comparable to that of Pt/C throughout the potential range of +0.70 to +0.90 V.

The fact that the AuMC-20% sample exhibited the best ORR activity among the series of AuMC nanocomposites implies a delicate balance between AuNPs loading and effective surface area. Whereas an increase of AuNPs loading is expected to lead to an increase of the number of catalytically active sites, as suggested in TEM measurements (Fig. 2), the effective surface area actually diminishes accordingly which hinders mass transfer of reaction species and thus reduces the ORR activity, as evidenced in BET measurements (Fig. 4). The AuMC-20% sample represents the optimal compromise between these two factors, and the performance was markedly better than that of gold nanoparticles (7 ± 2 nm in diameter) capped by a monolayer of 1,4-decylphenyl fragments where peroxides were the dominant product of oxygen reduction ($n \approx 2$),[40] but comparable to leading results in the literature involving, for instance, carbon nanotube-gold nanoparticle (dia. ~ 3 nm) hybrids,[41] within the context of number of electron transfer (n), kinetic current density and onset potential.

Finally, the durability of AuMC-10%, AuMC-20%, AuMC-30% and commercial Pt/C during ORR was evaluated by chronoamperometric measurements at +0.5 V. As shown in Fig. 6c, the cathodic current of AuMC-10%, AuMC-20% and AuMC-30% exhibited a loss of 28%, 31% and 27% after more than 8 h continuous operation, in comparison to 35% loss for the commercial Pt/C under the same experimental conditions. In fact, TEM measurements showed rather consistent structures of the AuMC hybrids with no obvious agglomeration and/or dissolution of the nanoparticles (Fig. S4†), whereas it is well-known that Pt/C displays marked agglomeration of the nanoparticles during ORR operation.[42] This suggests enhanced stability of the mesoporous carbon-supported AuNPs catalysts as compared to that of commercial Pt/C in alkaline solution.

Conclusions

In summary, ordered mesoporous carbon material supported AuNPs were prepared by simple pyrolysis. The intimate interactions between AuNPs and Z-SBA15 helped prevent the agglomeration of AuNPs during pyrolysis and provided highly active catalytic sites, which facilitated fast electron transfer and rapid mass transport. The AuMC-20% sample demonstrated a highly efficient electrocatalytic performance for ORR, within the context of onset potential, kinetic current density, and stability, as compared with AuNPs alone, mesoporous carbons, and commercial Pt/C. The strategy presented herein may be readily extended to prepare a wide range of electrocatalysts with desirable reactivity and extraordinary stability for ORR.

Acknowledgements

This work was supported by the National Recruitment Program of Global Experts. Z. H. T. acknowledges financial support from the Fundamental Research Funds for Central Universities (SCUT Grant No. 2015ZM012 and 2015PT026) and Guangdong Natural Science Funds for Distinguished Young Scholars (No. 2015A030306006). S. W. C. thanks the National Science Foundation for partial support of the work (CHE-1265635 and DMR-1409396).

References

1 M. K. Debe, *Nature*, 2012, **486**, 43–51.
2 A. Kraytsberg and Y. Ein-Eli, *Energy Fuels*, 2014, **28**, 7303–7330.
3 K. E. Swider-Lyons and S. A. Campbell, *J. Phys. Chem. Lett.*, 2013, **4**, 393–401.
4 S. Guo, S. Zhang and S. Sun, *Angew. Chem., Int. Ed.*, 2013, **52**, 8526–8544.
5 S. Proch, M. Wirth, H. S. White and S. L. Anderson, *J. Am. Chem. Soc.*, 2013, **135**, 3073–3086.
6 Z.-Y. Zhou, X. Kang, Y. Song and S. Chen, *J. Phys. Chem. C*, 2012, **116**, 10592–10598.
7 Y. Kang, X. Ye, J. Chen, Y. Cai, R. E. Diaz, R. R. Adzic, E. A. Stach and C. B. Murray, *J. Am. Chem. Soc.*, 2013, **135**, 42–45.
8 C. Zhang, S. Y. Hwang, A. Trout and Z. Peng, *J. Am. Chem. Soc.*, 2014, **136**, 7805–7808.
9 B. Lim, M. Jiang, P. H. C. Camargo, E. C. Cho, J. Tao, X. Lu, Y. Zhu and Y. Xia, *Science*, 2009, **324**, 1302–1305.
10 M. Liu, R. Zhang and W. Chen, *Chem. Rev.*, 2014, **114**, 5117–5160.
11 G. Wu and P. Zelenay, *Acc. Chem. Res.*, 2013, **46**, 1878–1889.
12 X. J. Liu, Y. C. Zhou, W. J. Zhou, L. G. Li, S. B. Huang and S. W. Chen, *Nanoscale*, 2015, **7**, 6136–6142.
13 P. G. Hu, Y. Song, L. M. Chen and S. W. Chen, *Nanoscale*, 2015, **7**, 9627–9636.
14 X. L. Sun, D. G. Li, Y. Ding, W. L. Zhu, S. J. Guo, Z. L. Wang and S. H. Sun, *J. Am. Chem. Soc.*, 2014, **136**, 5745–5749.
15 K. Uosaki, G. Elumalai, H. Noguchi, T. Masuda, A. Lyalin, A. Nakayama and T. Taketsugu, *J. Am. Chem. Soc.*, 2014, **136**, 6542–6545.
16 W. Tang, H. Lin, A. Kleiman-Shwarsctein, G. D. Stucky and E. W. McFarland, *J. Phys. Chem. C*, 2008, **112**, 10515–10519.
17 A. A. Herzing, C. J. Kiely, A. F. Carley, P. Landon and G. J. Hutchings, *Science*, 2008, **321**, 1331–1335.
18 C.-J. Jia, Y. Li, H. Bongard and F. Schuth, *J. Am. Chem. Soc.*, 2010, **132**, 1520–1522.
19 X. Nie, H. Qian, Q. Ge, H. Xu and R. Jin, *ACS Nano*, 2012, **6**, 6014–6022.
20 M. Turner, V. B. Golovko, O. P. H. Vaughan, P. Abdulkin, A. Berenguer-Murcia, M. S. Tikhov, B. F. G. Johnson and R. M. Lambert, *Nature*, 2008, **454**, 981–984.
21 Y. Zhu, H. Qian, M. Zhu and R. Jin, *Adv. Mater.*, 2010, **22**, 1915–1920.
22 Y. Liu, H. Tsunoyama, T. Akita, S. Xie and T. Tsukuda, *ACS Catal.*, 2011, **1**, 2–6.

23 W. Chen and S. Chen, *Angew. Chem., Int. Ed.*, 2009, **48**, 4386–4389.
24 Y. Li, J. T. Cox and B. Zhang, *J. Am. Chem. Soc.*, 2010, **132**, 3047–3054.
25 C. Jeyabharathi, S. Senthil Kumar, G. V. M. Kiruthika and K. L. N. Phani, *Angew. Chem., Int. Ed.*, 2010, **49**, 2925–2928.
26 H. Yin, H. Tang, D. Wang, Y. Gao and Z. Tang, *ACS Nano*, 2012, **6**, 8288–8297.
27 G. Goncalves, P. A. A. P. Marques, C. M. Granadeiro, H. I. S. Nogueira, M. K. Singh and J. Grácio, *Chem. Mater.*, 2009, **21**, 4796–4802.
28 C. Lin, Y. Song, L. Cao and S. Chen, *ACS Appl. Mater. Interfaces*, 2013, **5**, 13305–13311.
29 J. Qi, J. Chen, G. Li, S. Li, Y. Gao and Z. Tang, *Energy Environ. Sci.*, 2012, **5**, 8937–8941.
30 C. Jin, X. Cao, F. Lu, Z. Yang and R. Yang, *ACS Appl. Mater. Interfaces*, 2014, **6**, 847–853.
31 B. Fang, J. H. Kim, M.-S. Kim and J.-S. Yu, *Acc. Chem. Res.*, 2013, **46**, 1397–1406.
32 B. Fang, J. H. Kim, M. Kim and J.-S. Yu, *Chem. Mater.*, 2009, **21**, 789–796.
33 S. Jun, S. H. Joo, R. Ryoo, M. Kruk, M. Jaroniec, Z. Liu, T. Ohsuna and O. Terasaki, *J. Am. Chem. Soc.*, 2000, **122**, 10712–10713.
34 Z. Wu, J. Chen, P. Zhang and R. Jin, *Adv. Funct. Mater.*, 2011, **21**, 177–183.
35 X. Liu, L. Li, W. Zhou, Y. Zhou, W. Niu and S. Chen, *ChemElectroChem*, 2015, **2**, 803–810.
36 W. Niu, L. Li, X. Liu, N. Wang, J. Liu, W. Zhou, Z. Tang and S. Chen, *J. Am. Chem. Soc.*, 2015, **137**, 5555–5562.
37 K. Zhou, W. Zhou, X. Liu, Y. Wang, J. Wan and S. Chen, *ACS Appl. Mater. Interfaces*, 2014, **6**, 14911–14918.
38 G. Q. He, Y. Song, K. Liu, A. Walter, S. Chen and S. W. Chen, *ACS Catal.*, 2013, **3**, 831–838.
39 Y. Song and S. W. Chen, *ACS Appl. Mater. Interfaces*, 2014, **6**, 14050–14060.
40 F. Mirkhalaf and D. J. Schiffrin, *Langmuir*, 2010, **26**, 14995–15001.
41 A. Morozan, S. Donck, V. Artero, E. Gravel and E. Doris, *Nanoscale*, 2015, **7**, 17274–17277.
42 Z. Y. Zhou, X. W. Kang, Y. Song and S. W. Chen, *Chem. Commun.*, 2012, **48**, 3391–3393.